Solid-State Field-Assisted Ion Exchange (Ag → Na) in Soda–Lime Float Glass: Tin Versus Air Side

Mattia Biesuz,* Gino Mariotto, Michele Cassetta, Ovidiu Ersen, Dris Ihiawakrim, Petr Haušild, Paolo Giopato, Alessandro Martucci, Mauro Bortolotti, Vincenzo M. Sglavo, and Gian D. Sorarù

The application of a DC current allows fast (few minutes) $Ag^+ \rightarrow Na^+$ ion exchange in soda–lime–silicate (SLS) glass. The effect of processing parameters, electric current, and treating time is studied on both air and tin sides of SLS float glass, and non-Fickian diffusion is revealed. It is shown that ion exchange kinetics are similar on both sides and the tempering process results in similar mechanical properties (crack formation probability after Vickers indentation, hardness, and Young's modulus). However, the structure/microstructure of the tin and air sides is hugely different. In particular, clear silver nanoclustering takes place on the tin side, resulting in ≈8 nm metallic particles in the vicinity of the surface. The formation of nanoparticles is also coupled with a deep structural reorganization of the amorphous network and the Q^n units. The nanoparticles' size decreases moving from the surface to the interior of the glass. Silver nanoparticles are also detected on the air side, although their density and size are largely reduced. Whereas the mechanical properties measured on the air and tin side are similar, significative differences are observed in terms of optical properties.

1. Introduction

The rapid development of touch screen devices over the last decade has led to a renewed interest in glass surface engineering.[1,2] On one hand, chemical modification of the glass surface can improve mechanical properties (chemical tempering) by exchanging Li^+ or Na^+ in the glass composition with larger alkaline ions (typically Na^+ or K^+). On the other hand, the introduction of specific elements on the glass surface (silver, copper, zinc, and others) can activate desirable antimicrobial (or even virucidal[3]) properties.[4–8] In this context, Ag is among the most studied elements because it combines biocidal activity, a moderate strengthening and interesting optical properties: being silver relatively heavy, it causes a local variation of the refractive index that can be used to obtain waveguides.[9–11]

Silver is usually inserted into soda–lime glass through the ion exchange process, where the glass is soaked into a molten

M. Biesuz, P. Giopato, M. Bortolotti, V. M. Sglavo, G. D. Sorarù
Department of Industrial Engineering
University of Trento
Via Sommarive 9, 38122 Trento, Italy
E-mail: mattia.biesuz@unitn.it

G. Mariotto, M. Cassetta
Department of Computer Science
University of Verona
Strada Le Grazie 15, 37034 Verona

O. Ersen, D. Ihiawakrim
Institut de Physique et Chimie des Matériaux de Strasbourg
Université de Strasbourg
CNRS
UMR 7504
F-67000 Strasbourg, France

P. Haušild
Faculty of Nuclear Sciences and Physical Engineering
Department of Materials
Czech Technical University in Prague
Trojanova 13, 120 00 Prague, Czechia

A. Martucci
Department of Industrial Engineering
University of Padova
Via Francesco Marzolo 9, 35131 Padova, Italy

V. M. Sglavo
National Council of Research
Institute of Photonics and Nanotechnologies
Via alla Cascata 56/C, 38123 Trento, Italy

The ORCID identification number(s) for the author(s) of this article can be found under https://doi.org/10.1002/adem.202201572.

silver-containing salt bath at ≈400 °C.[2,8,12–18] Such temperature is high enough to allow M^+ diffusion but not to cause any distortion or stress relaxation. Ag^+ ions, driven by the concentration gradient, migrate from the salt into the glass while an opposite alkaline ions flux occurs from the glass into the molten salt. This process is very slow and typically requires several hours. To overcome this limitation, it can be accelerated by applying an electric field that introduces an extra driving force for ion exchange (field-assisted ion exchange),[2,12,19] thus decreasing the treating time down to a few minutes. Nevertheless, also this process presents some limitations: 1) it makes use of large amounts of Ag salts which are rather expensive and 2) it is not possible to treat the borders of the sample because the two faces need to be electrically separated and 3) it is not possible to selectively treat only well-defined regions of the component to produce textures (the salt in the molten state is difficult to be confined). An attractive alternative is the use of solid-state field-assisted ion exchange (SS_FAIE), also known as dry field-assisted ion exchange. Here, the molten Ag salt bath is substituted by a metallic Ag electrode;[20–23] Ag is connected to the positive terminal of a DC power source and substitutes the alkali ions moving into the glass toward the cathode.

Said technique typically inserts Ag^+ ions[20,24] in the glass structure; however, Ag^+ can be quite easily converted into metallic Ag colloids by annealing the ion-exchanged component in reducing conditions or even in air.[18,25–30] Some researchers reported that the as-exchanged glass can already contain metallic silver in sub-nanoclusters[16] or even nanoclusters[31,32] without postannealing. The formation of metallic nanoclusters[16] is indeed a matter of interest as they found several applications in the field of plasmonics,[15,27] optoelectronics,[25,33] photovoltaic,[34] and medicine.[35] Moreover, colloids embedded within a dielectric, transparent, and isotropic matrix (as glass is) offer fascinating optical properties[13,14,17,25,27,36–38] related to the surface plasmon resonance absorption.

It is known that soda–lime–silicate (SLS) float glasses (i.e., the most diffuse oxide glass composition) possess strong asymmetry between the two faces. This is related to the manufacturing process, where the silicate melt "floats" over a molten tin bath. Hence, we can distinguish the "tin side" in contact with molten Sn and the "air side" facing the furnace atmosphere. The tin side contains a certain amount of Sn (up to ≈1 at%) which can penetrate down to ≈10 μm.[39–41] Tin possesses different oxidation states within the glass network; Sn^{2+} is dominant just beneath the surface in contact with the molten metal bath, whereas Sn^{4+} becomes more relevant moving toward the bulk. The presence of this chemical asymmetry is thought to affect conventional ion exchange processes ($K^+ \rightarrow Na^+$), potassium diffusion being partially hindered by the presence of Sn,[42,43] although this conclusion is still controversial.[44] On the other hand, to the best of our knowledge, no literature data on the effect of tin versus air side are available for field-assisted ion exchange processes involving silver, despite Ag^+ ion incorporation into float glass is currently gaining increasing technical relevance. Till now thin glass sheets for touch screen applications (where the antimicrobial activity of silver is particularly important) were manufactured by down-drawn only, float process being employed for thicker artifacts. In 2019, Pilkington launched NSG Glanova, the first commercial thin float glass sheet;[45,46] thus, we can foresee that in the next few years float glass will gain increasing relevance in touch applications which should be ideally self-sterilizing.

The present work aims at filling this gap in the scientific literature by providing a comparison between field-assisted $Ag^+ \rightarrow Na^+$ ion exchange on tin and air side of SLS float glass. In particular, silver penetration, optical transmittance structural modifications on the two sides of the glass are examined and compared. Preliminary results also provide an insight into the effect of ion exchange on the resistance to flaws formation (crack formation probability).

2. Results

The electric quantities/properties recorded during field-assisted ion exchange are reported in **Figure 1**. We can observe that no significant differences in the electric parameters can be detected when samples treated on the tin and air side are compared. When the electric current is 5 mA cm^{-2}, both electric field and conductivity remain barely constant during the entire process. If higher currents are applied (10 or 20 mA cm^2), an electric field spike is observed at the beginning of the process; then the field decreases
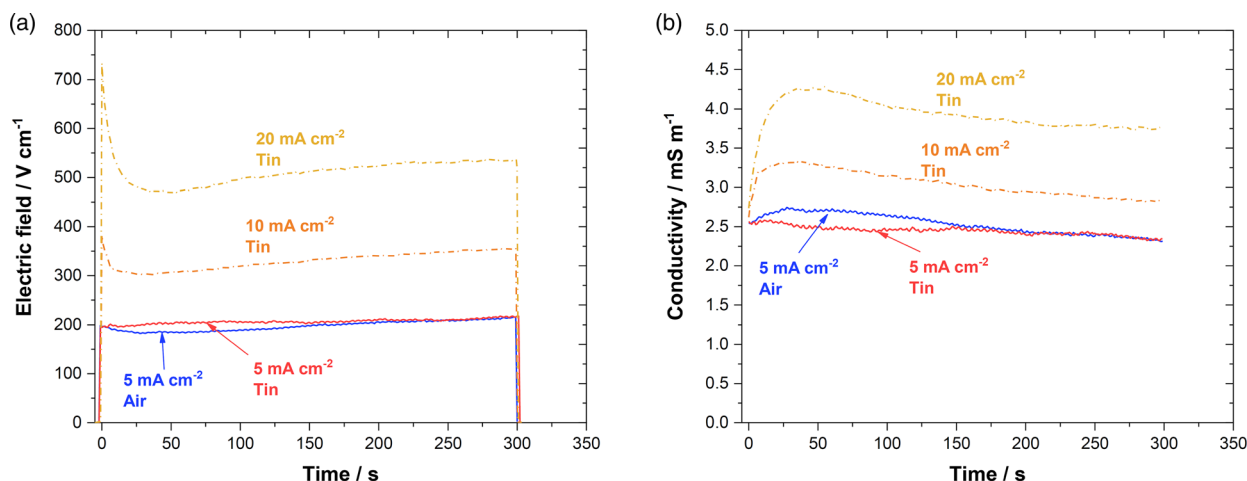

Figure 1. a) Electric conductivity and b) field recorded during field-assisted ion exchange at 380 °C.

**ADVANCED
SCIENCE NEWS**

www.advancedsciencenews.com

**ADVANCED
ENGINEERING
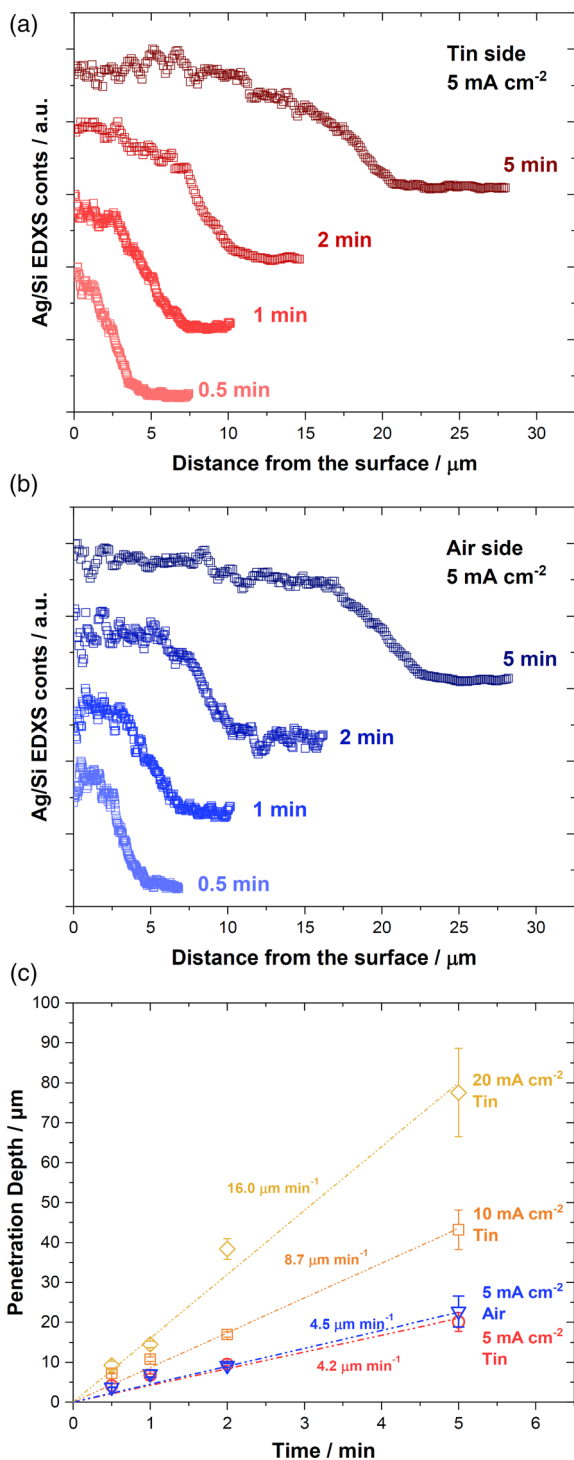MATERIALS**

www.aem-journal.com

Figure 2. Silver concentration profiles (determined by EDXS) on field-assisted ion-exchanged glasses on a) tin and b) air side. The silver EDXS counts were normalized to the silicon ones and offset for clarity (the silver concentration is always equal to zero in the bulk). c) Penetration depth of silver as a function of treating time for different current densities.

(first 30–60 s) and finally slightly increases again. The opposite behavior is observed for the electrical conductivity which

typically reaches a maximum ≈ 40 s after the beginning of the process.

Figure 2 shows the silver concentration profiles after field-assisted ion exchange in samples treated with 5 mA cm^{-2} for different times (0.5–5 min). For both thin (a) and air (b) sides silver concentration remains substantially constant for a certain depth which increases with the treatment duration and then decreases to zero. Small fluctuation in the Ag concentration can be primarily ascribed to the nonperfectly flat geometry of the fracture surface to zero.

The Ag penetration depths are reported in Figure 2c as a function of the treating time. We can observe that there is a substantially linear relationship between the exchange time and silver penetration depth for both tin and air sides (≈ 4 μm min^{-1}) under a current density of 5 mA cm^{-2}. In addition, no statistically significant differences between the air and tin side can be detected.

Some additional samples were exchanged on the tin side with higher current densities for comparison (panel (c) of the same figure). We can observe that the Ag penetration rate increases with the current density, being ≈ 4, 8, and 16 μm min^{-1} under 5, 10, and 20 mA cm^{-2}, respectively. There is, therefore, a substantially linear relation between the exchange rate and the current density.

The XRD patterns of the ion-exchanged materials do not show any clear crystalline feature and only a broad amorphous hump appears (**Figure 3**). However, a clear shift of such amorphous feature to higher 2θ is observed ($\approx 1°$ and $\approx 5°–6°$ after 0.5 and 5 min treatment under 5 mA cm^{-2}) for both tin and air side-treated samples. For the samples exchanged on the tin side, most of the alterations of the diffraction spectrum are already achieved after 5 min treatment under 5 mA cm^{-2} and only marginal modification can be pointed when higher currents are applied. Interestingly, some differences can be highlighted between the air and tin side in the high angle region of the amorphous hump: whereas the hump descends quite sharply on the air side (it lasts at 2θ–40°, Figure 3b), it appears very broad with a gentle slope on the tin side (it extends almost to 2θ–50°, Figure 3c).

Typical cross-polarized (HV) reduced Raman spectra of the ion-exchanged glasses (5 min, 5 mA cm^{-2}), recorded in the low-wavenumber region below 100 cm^{-1}, are shown in **Figure 4**. All spectra are characterized by the presence of a broad Raman peak between $\approx 14–22$ and $\approx 27–35$ cm^{-1} for the tin (a) and the air (b) side, respectively. The peak position depends on the distance from the surface and it progressively shifts toward higher wavenumbers moving from the surface to the bulk. Correspondingly, the peak width progressively broadens, although keeping the same spectral profile even at the deepest penetration depths of silver. The Raman peaks are quite clear and well defined on the tin side (high signal-to-noise ratio), whereas they appear much noisier on the air side. As such, it was not possible to acquire spectra at a depth exceeding 10 μm in the case of the samples treated on the air side.

The TEM results are shown in **Figure 5**. The micrographs clearly show the presence of crystalline spherical nanoprecipitates (less than 10 nm) within the glass matrix (Figure 5). The resulting SAED pattern is consistent with an FCC crystal structure with a cell parameter of about 0.4 nm (inset of Figure 5a).

The FTIR spectra obtained on the tin and air side of the pristine and ion-exchanged glass are shown in **Figure 6**. All the spectra present a clear vibrational feature close to 800 cm^{-1} associated
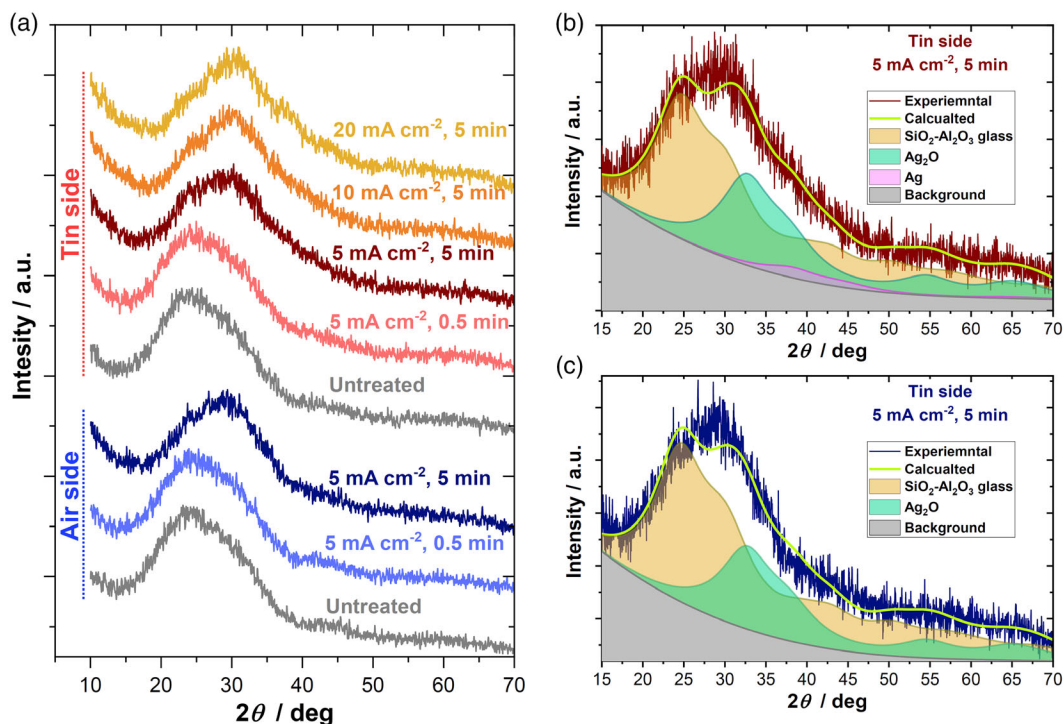
Figure 3. a) XRD patterns of SS_FAIE SLS glass at different processing conditions; refined patterns on the b) tin and c) air side.
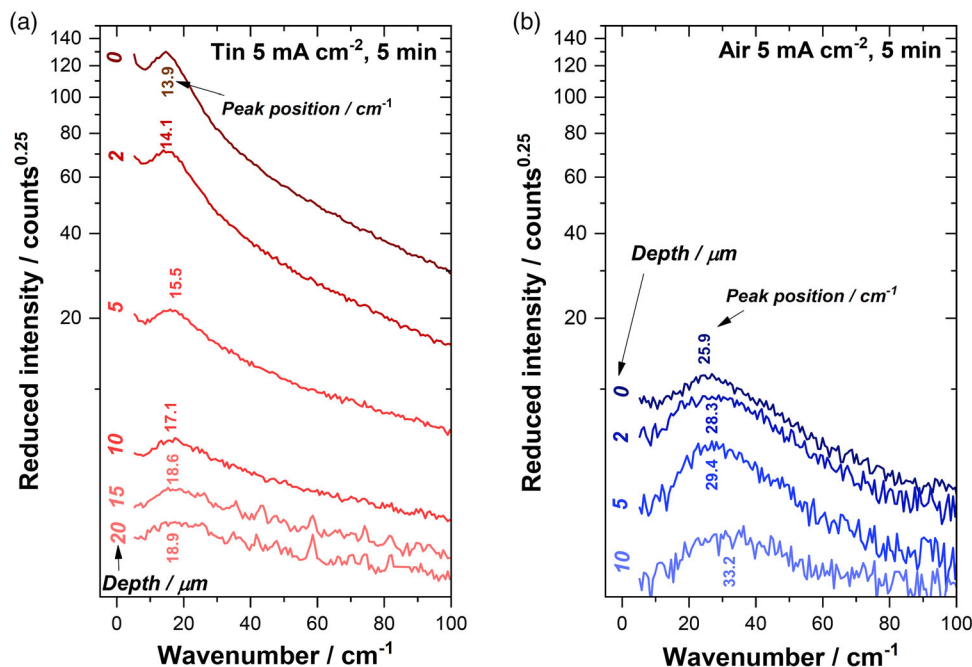

Figure 4. Low-frequency reduced Raman spectra (calculated using Equation (6)) collected at different depth on FAIE SLS glass on a) tin and b) air side.

with the bending of Si—O bonds in silicate rings.[47] Moreover, a broad feature associated with the Si—O stretching can be detected between 950 and 1250 cm^{-1}.[47–49] This hump can be deconvoluted using four Gaussian components whose position, area, and width change with the ion-exchange process (**Table 1**).

Whereas the changes of the IR band are relatively small for the ion exchange process carried out on the air side, more relevant modifications can be highlighted on the tin side.

Some optical features of the ion-exchanged materials are reported in **Figure 7**. The glasses exchanged on the tin side

2201572 (4 of 12)
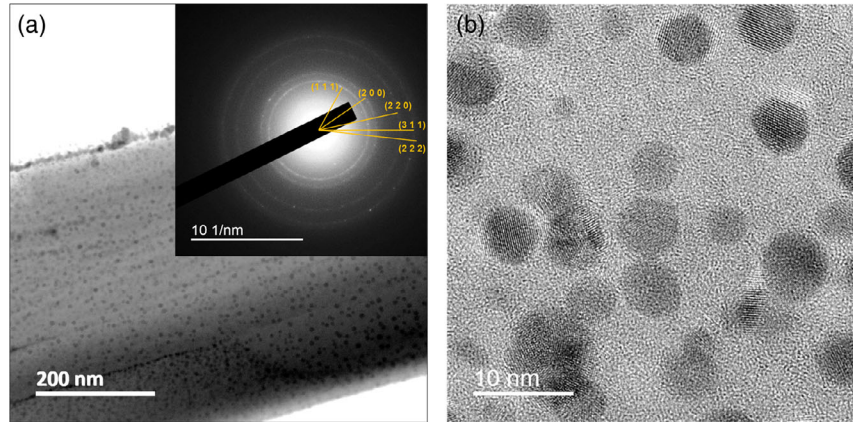
Figure 5. a) Typical TEM and b) HRTEM micrographs of the surface of FAIE tin side of SLS glass (5 mA cm^{-2}, 5 min). The inset in (a) reports the SAED spectrum.
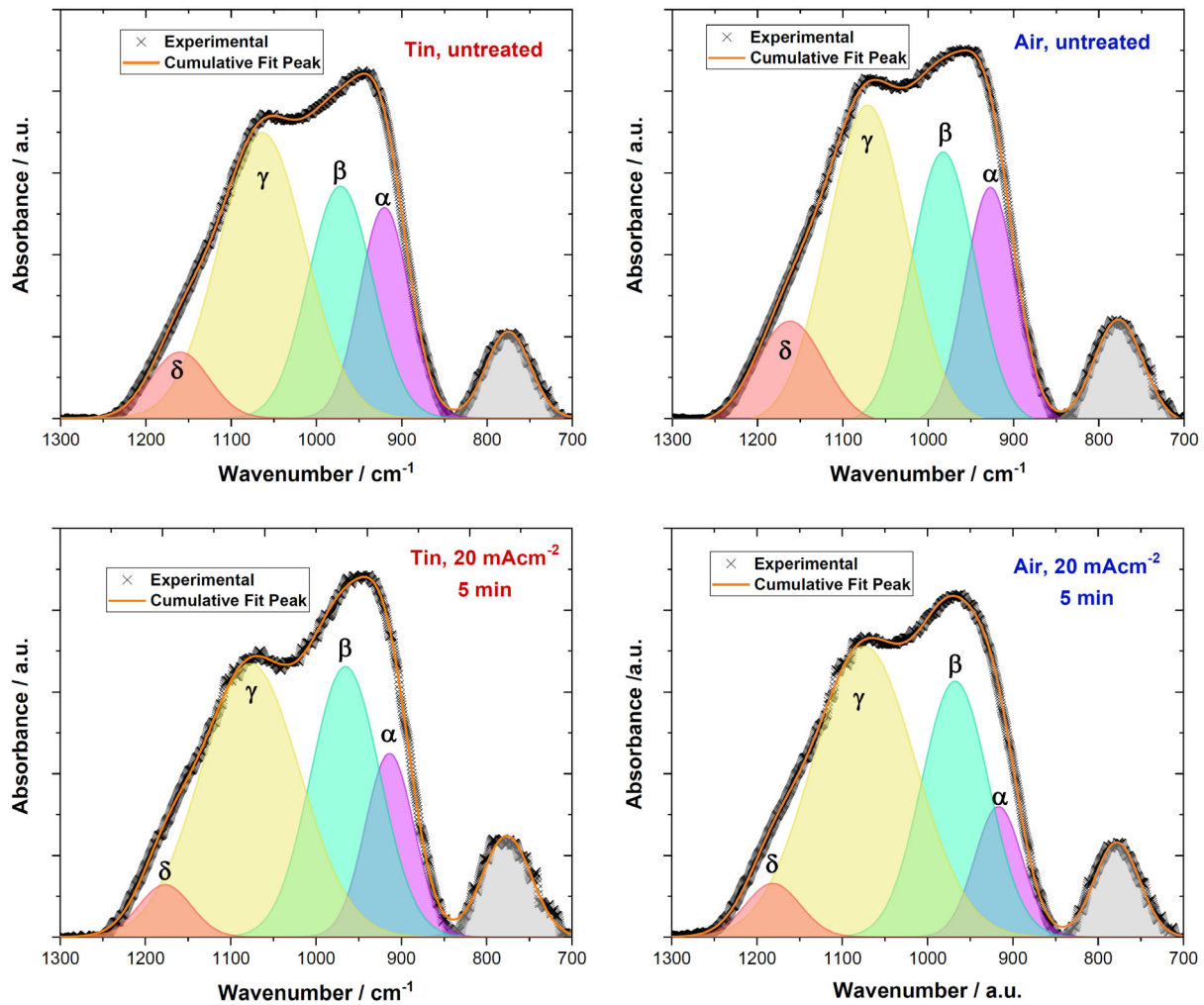
Figure 6. FTIR spectra of SLS glass before and after FAIE.

present a brownish coloration which becomes more evident and darker by increasing the treating time (and current). On the other hand, the glasses exchanged on the air side remain substantially transparent (or pale yellow in the case of prolonged treatments). The differences in terms of optical properties are confirmed by the absorbance spectra in the UV/vis (Figure 7c,d). The untreated

Table 1. Deconvoluted components of the FTIR spectra in Figure 7.

		Tin, untreated	Tin, FAIE	Air, untreated	Air, FAIE
α	Position [cm^{-1}]	920	914	927	917
	FWHM [cm^{-1}]	58	57	59	56
	Area [%]	19.3	16.6	19.5	11.0
β	Position [cm^{-1}]	972	965	982	968
	FWHM [cm^{-1}]	75	81	74	79
	Area [%]	27.7	34.7	28.0	30.5
γ	Position [cm^{-1}]	1064	1077	1071	1074
	FWHM [cm^{-1}]	101	116	93	120
	Area [%]	45.8	50.5	41.2	53.2
δ	Position [cm^{-1}]	1151	1177	1162	1181
	FWHM [cm^{-1}]	68	61	79	64
	Area [%]	7.2	5.1	11.3	5.2

glass is substantially transparent in the whole visible spectrum, whereas the absorbance sharply increases below $\approx$330 nm

because of the band edge absorption. After ion exchange on the air side, the absorption spectra marginally changed. The main differences consist of a moderate increase of the absorbance in the blue part of the visible spectrum ($\approx$400–500 nm) and a small redshift (a few nm) of the band edge. These features become stronger as the exchange time increases. Despite similar phenomena can be observed also in the glasses exchanged on the tin side, their magnitude is definitively different. In particular, the absorption of visible light is strongly enhanced in the blue region. Nonetheless, the absorption region appears very wide-spanning also to the red. The effect appears definitively enhanced when increasing the treating time and current. In particular, the samples treated in the most severe conditions appear to show a very broad hump in the absorption spectrum centered around 450 nm.

Some differences between the samples exchanged on the air and tin side can also be detected under UV irradiation (Figure 7a,b). The samples were illuminated in two different modes: first, the UV lamp shined on the ion-exchanged side of the sheet; then, the samples were placed upside-down and the illumination came from the untreated side (i.e., the UV lamp
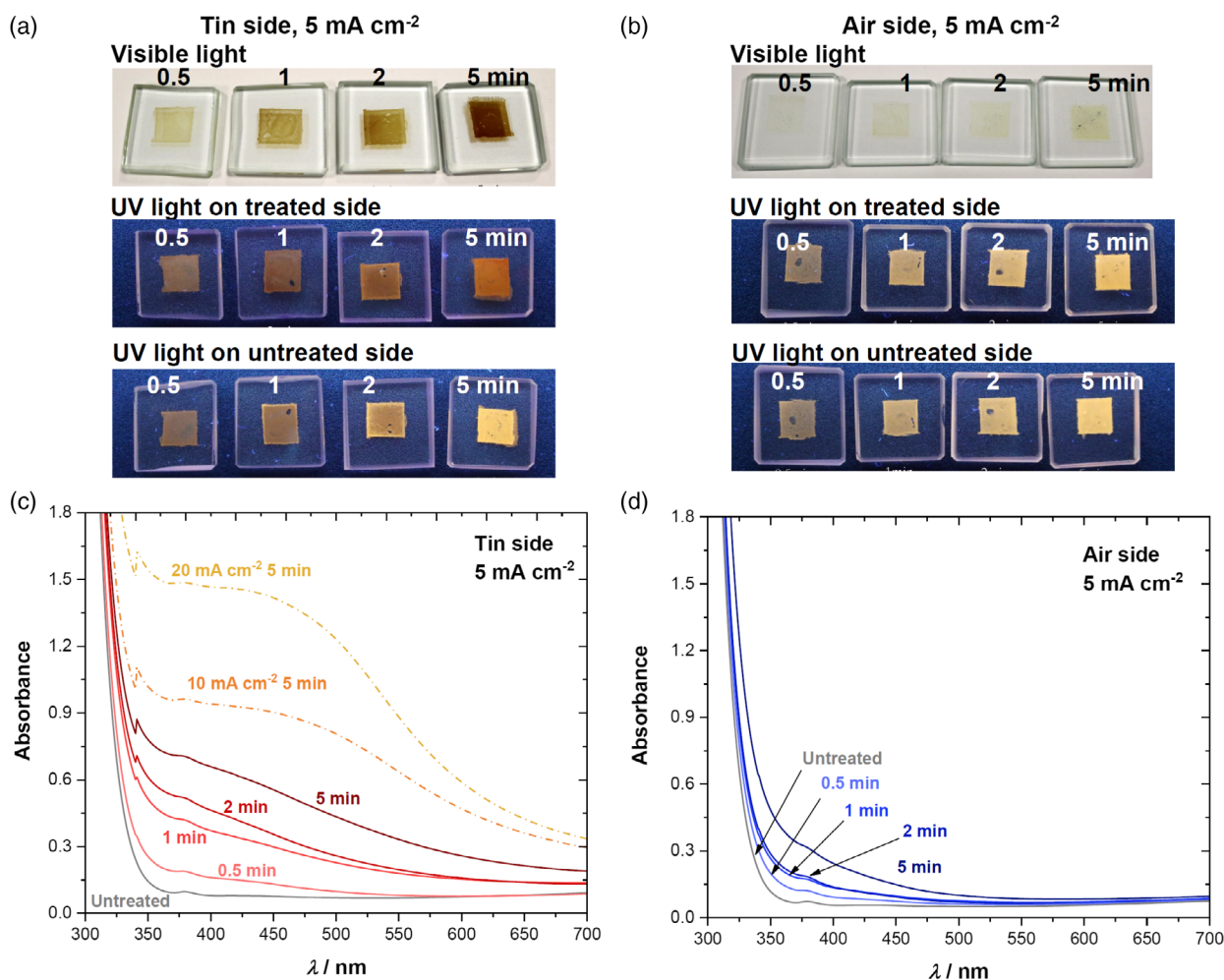

Figure 7. Photographs of Ag-exchanged glasses under visible and UV irradiation; a,b) refer to samples exchanged on tin and air side, respectively. UV/visible absorbance as a function of the wavelength for glasses exchanged on c) tin and d) air side.
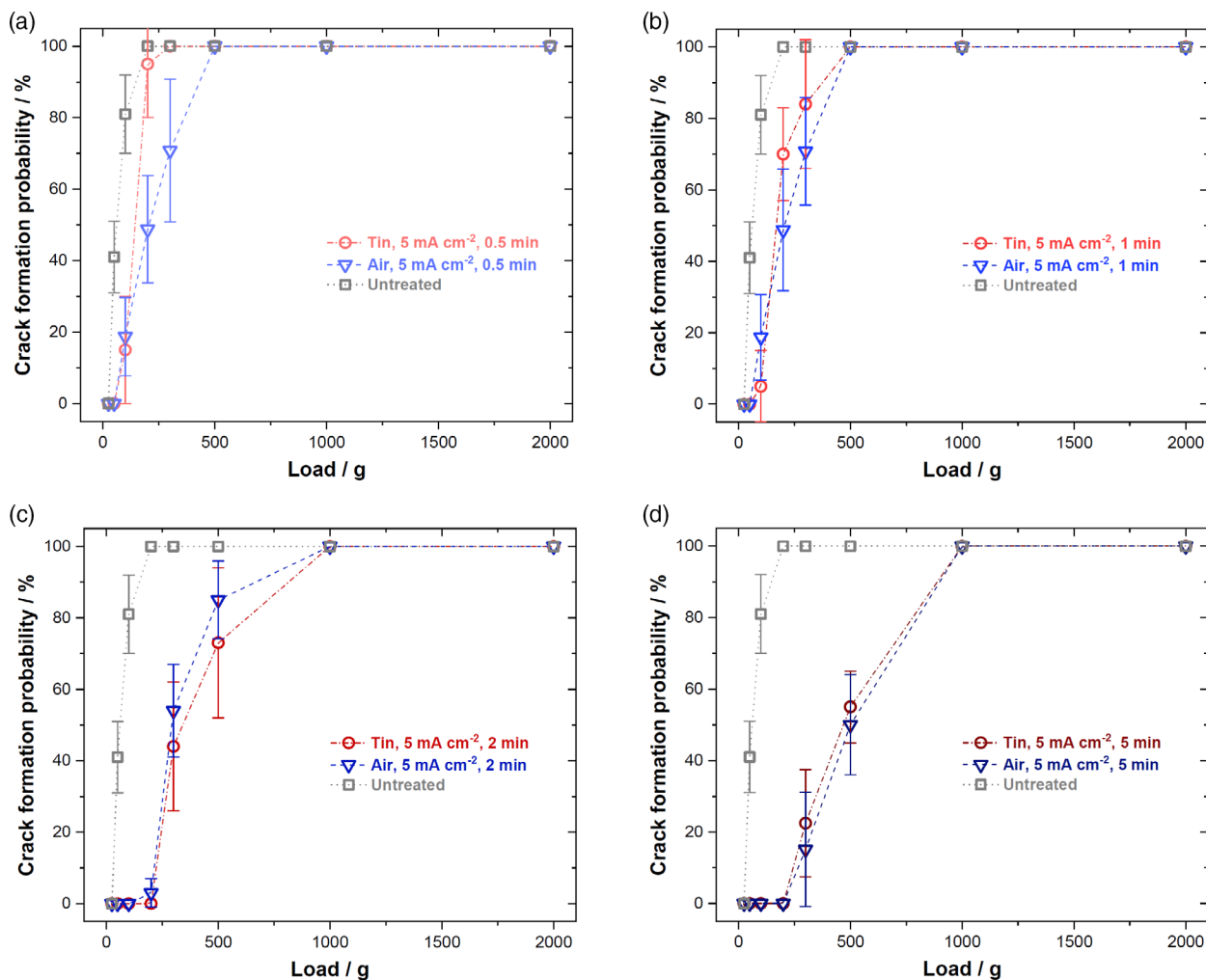
**ADVANCED
SCIENCE NEWS**

www.advancedsciencenews.com

**ADVANCED
ENGINEERING
MATERIALS**

www.aem-journal.com

Figure 8. Crack formation probability as a function of the indentation load (Vickers indenter) in glasses exchanged on tin and air side under 5 mA mm^{-2} for a) 0.5, b) 1, c) 2, and d) 5 min.

was placed on the air side for the samples exchanged on the tin one and vice versa). The glasses treated on the air side show a bright yellowish luminescence regardless of the position of the UV lamp. Conversely, those treated on the tin side for 2 and 5 min possess luminescent properties strongly dependent on the lamp position. If the lamp shines on the tin side, they produce a quite dark, red/orange luminescence, but when they are placed upside-down (and the lamp shines on the air side) the luminescence becomes bright and yellowish, relatively similar to that recorded on the samples exchanged on the air side. The sample treated for 0.5 min on the tin side always shows a reddish weak luminescence, regardless of the lamp position; the specimen treated for 1 min shows an intermediate behavior.

The FAIE causes a detectable reduction of the crack formation probability after Vickers indentation on both sides of the glass, the effect becoming more significant for longer treating time (**Figure 8**). In particular, the onset for crack formation increases from 50 g up to 300 g in the case of the longest treatment (5 min under 5 mA cm^{-2}). The strengthening of the glass surface

appears similar on both sides (Figure 8). While FAIE induces a remarkable reduction of the flaw formation probability, it does not change significantly other mechanical properties such as elastic modulus and hardness (**Figure 9**).

3. Discussion

The electric data in Figure 1 do not show significant difference between tin and air side. The stability of the voltage and conductivity during the entire process under small current densities (5 mA cm^{-2}) confirms that the electrodes are nonion blocking, thus implying that silver is electrochemically active and able to exchange ions with the glass. In fact, if Ag acted as an ion blocking electrode, then a rapid drop of the electrical conductivity would take place due to the formation of an ion depletion layer at the positive terminal.[50–52] The small increase of electric conductivity with time can be very likely attributed to a modest Joule heating of the specimen (estimated at ≈10 and 21 °C when the applied current is 10 and 20 mA cm^{-2}, respectively; see Supporting Information for further details).

ADVANCED
SCIENCE NEWS

www.advancedsciencenews.com
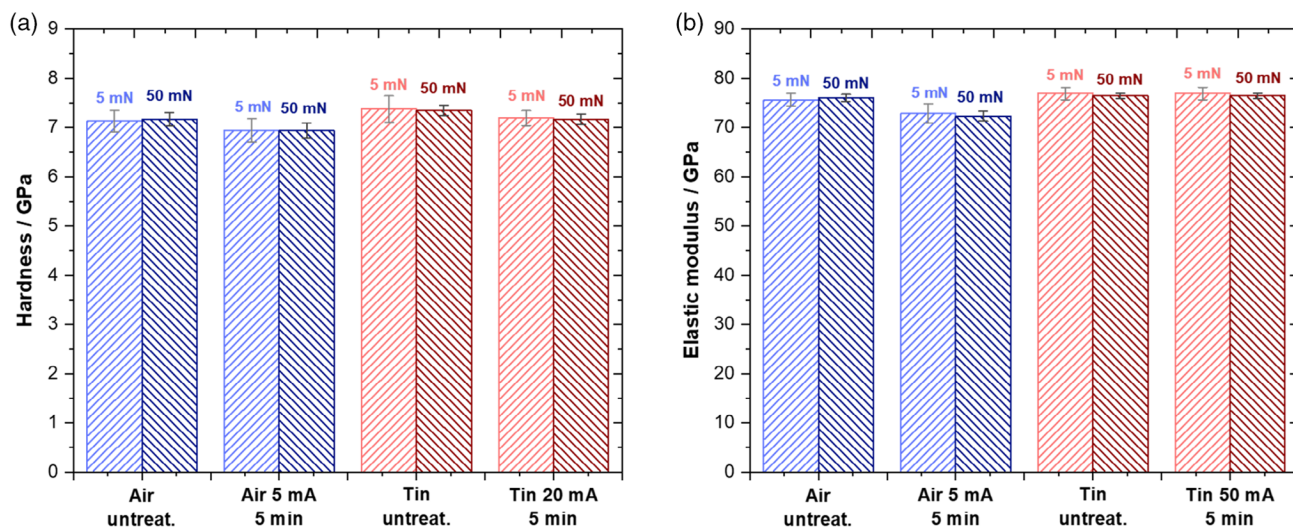
ADVANCED
ENGINEERING
MATERIALS

www.aem-journal.com

Figure 9. a) Hardness and b) elastic modulus of pristine and FAIE SLS float glass on tin and air side with different indentation loads.

The concentration profile shape and the linear relation between penetration depth and processing time reveal a non-Fickian diffusion (Figure 2) as expected when the ion exchange is driven by an electrical field.[53] The results also show that the float glass sheet side does not affect significantly the kinetics of field-assisted ion exchange.

The penetration of silver can be modeled assuming a linear relation with treating time and current. Fitting the experimental results, we can estimate the penetration depth (l) as

$$l \approx 0.8\,jt \tag{1}$$

where t is the treating time [min] and j is the current density [mA cm^{-2}]. This equation can be compared with the moles of Na$^+$ that are expected to be displaced under the effect of the electric current for each cm^2 of surface (i.e., Jt/F, F being the Faraday constant). From the glass composition and the glass density (2.5 g cm^{-3}), we can estimate the penetration depth (d^*) assuming that the whole current is brought by Na$^+$ and each Na$^+$ is substituted by a silver ion in the exchanged layer

$$l^* \approx 0.56\,jt \tag{2}$$

Equation (2) captures, as a first approximation, the experimental penetration, suggesting that the proposed mechanism is substantially valid (i.e., silver ions completely substitute sodium displaced by the electric current). On these bases, the penetration kinetics result unaffected by the side of the float glass sheet (i.e., air vs tin) as long as Na concentration is homogeneous throughout the glass cross section. Nonetheless, we can remark that Equation (2) underestimates the measured penetration of silver. The origin of this partial inconsistency is likely related to the fact that Ag concentration profiles are not really "step-like", but there is a few microns thick region where silver penetrates only partially to replace Na.

Despite the penetration kinetics are substantially the same on the air and tin side, the structural and microstructural features of the exchanged glass appear quite different. In particular, the

low-frequency Raman spectra reveal the presence of nanocrystals on both air and tin sides, although with remarkable different characteristics in terms of particle size and density. We can identify these nanocrystals as metallic silver after TEM/SAED results. The low-frequency Raman peak in Figure 4, therefore, originates from the Raman active spheroidal vibrational modes of Ag nanoclusters embedded/incorporated in the glass matrix as theorized in the seminal work of Lamb.[54,55] The $l = 0$ and $l = 2$ particle modes are characterized by typical frequencies (ω) which are proportional to the inverse of the particle diameter (d). Starting from the material sound velocities (transverse v_t and longitudinal v_l) is possible to estimate the diameter as[56]

$$\omega_0 = \frac{k_0 v_t}{dc}; \quad \omega_2 = \frac{k_2 v_l}{dc} \tag{3}$$

where $k_{0,2}$ are constants depending on the v_l/v_t ratio within and on the boundary of the particle, d is the nanoparticle diameter, c is the light velocity in the vacuum, while $v_t = 1660$ m s^{-1} and $v_l = 3650$ m s^{-1} are the transverse and longitudinal sound velocities, respectively, in metallic silver. Accordingly, **Figure 10** reports the estimated Ag nanocrystals size. We can observe that 1) the Ag nanocrystals diameter on the tin side doubles that on the air side and 2) the nanocrystals size tends to be reduced moving toward the core of the glass, this being particularly evident on the tin side. Moreover, we can infer that the nanocrystals concentration is much larger on the tin side. In fact, the Raman nanoparticle signal-to-noise ratio (Figure 4) on the tin side is much larger than that on the air one, thus evidencing a much larger concentration of scattering centers. This is further confirmed by the XRD spectra (Figure 3) which reveal the presence of a high-angle tail (extending above $2\theta = 40°$) which can be attributed to "amorphous-like" metallic silver only on the tin side. The absence of clear nanocrystalline diffraction peaks can be likely attributed to the small crystallite size combined with a relatively low crystallite density. The particle size estimated on the surface of the tin side using the low-frequency Raman is $\approx$8 nm and 3.5 nm using the longitudinal ($l = 2$) and transversal ($l = 0$)
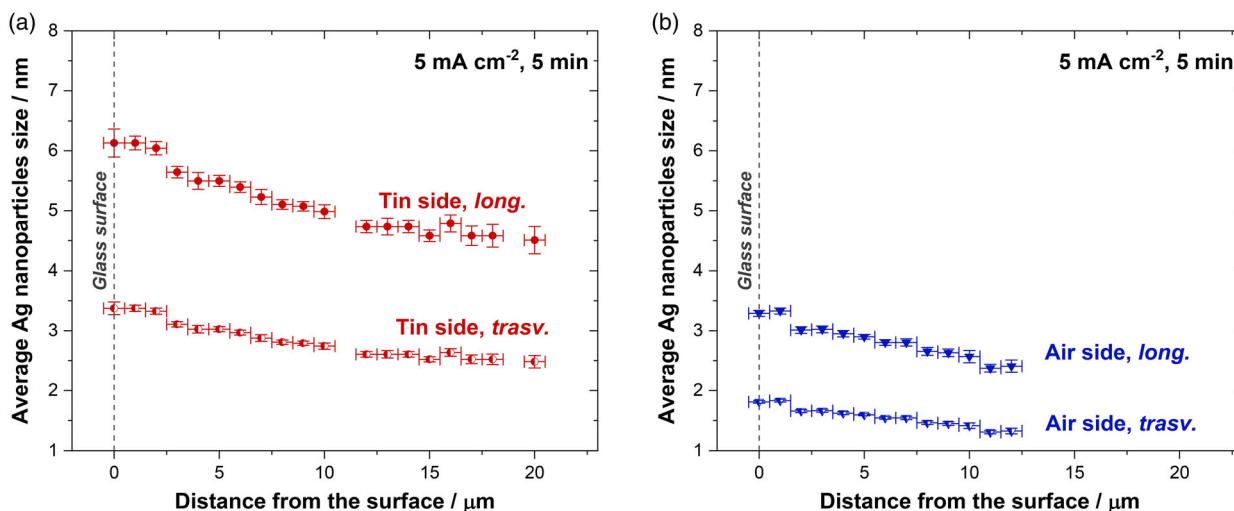
2201572 (8 of 12)

**ADVANCED
SCIENCE NEWS**

www.advancedsciencenews.com

**ADVANCED
ENGINEERING
MATERIALS**

www.aem-journal.com

Figure 10. nc-Ag particle size on the tin and air side of FAIE (5 mA cm^{-2}, 5 min) SLS glass as calculated from Equation (3) using the spectra in Figure 4.

vibrational mode equations, respectively. The nanoparticles diameter calculated in the transversal mode is not in agreement with TEM micrographs (Figure 5), whereas the estimation in logintudinal mode seems to provide a reasonable approximation of the observed nanostructures. Concerning larger particles, it is worth noting that for nanoparticles having $d \gtrsim 10$ nm, we will get frequencies too low to be clearly observed, due to the much strong overlapping elastic scattering.[57]

The formation of Ag nanoparticles is related to a reduction process of the silver ions which can be induced by the transition metals present in the glass composition. In particular, considering the glass composition, Fe^{2+} (both on tin and air side) and Sn^{2+} (only in the tin side) are the most reasonable reducing agents for Ag^+. To confirm this from a thermochemical perspective, we calculated ΔG^0 for

$$Ag_2O + SnO \rightarrow 2Ag + SnO_2 \tag{4}$$

and

$$Ag_2O + 2FeO \rightarrow 2Ag + Fe_2O_3 \tag{5}$$
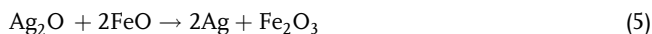
using the thermochemical data available in refs. [58,59]. The results point out that the first reaction is spontaneous ($\Delta G^0 < 0$) over a wide temperature range and specifically $\Delta G^0 \approx -250$ kJ at the ion exchange temperature (**Figure 11**). The large and negative ΔG^0 points out that silver ions are converted into metallic silver until all the Sn^{2+} oxidizes to Sn^{4+}. On these bases, silver nanocrystals can effectively form on the tin side of the float glass. As the tin concentration is expected to reduce moving from the surface to the core, this results in the observed progressive reduction of the nanocrystals size and concentration.

Also, Fe^{2+} can act as a reducing agent for Ag^+, though the driving force for the reaction is lower (Figure 11). The oxidation of Fe^{2+} is most likely responsible for the limited presence of nc-Ag also on the air side. However, the magnitude of the reduction on the air side is definitely more limited because of the differences in the reducing agent concentration. In fact, according to the nominal composition of the glass, the iron oxide load is below 0.2 wt%. With some simple stoichiometric calculations, assuming that 1) all the iron is in the 2+ state before ion exchange and 2) the atomic Ag concentration is equal to that of Na in the pristine glass, we can calculate that less than 1% of the exchanged Ag ions can be converted into metallic Ag by the oxidation of iron. On the other hand, the Sn concentration on the tin side can be up to 1 at% on the surface and most of tin is in the 2+ state in the first microns.[39–41] Thus, we can estimate that up to ≈20% of the exchanged Ag ions can be converted into metallic silver on the tin side surface.

In addition to the formation of metallic nanoclusters, the ion exchange process caused a structural reorganization of the glass as pointed out by the deconvolution of the FTIR–ATR spectra (Figure 6). In general, after ion exchange, the Si—O asymmetric
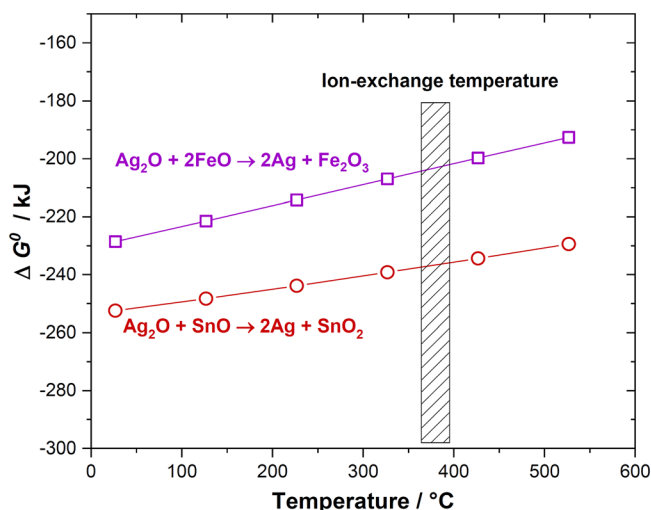

Figure 11. Gibbs free energy variation for silver reduction assisted by $Sn^{2+} \rightarrow Sn^{4+}$ oxidation as a function of temperature. Thermochemical data are taken from refs. [58,59].

**ADVANCED
SCIENCE NEWS**

www.advancedsciencenews.com

**ADVANCED
ENGINEERING
MATERIALS**

www.aem-journal.com

peak broadens, thus reflecting a larger variability of the bonding angles. The attribution of the different components of the FTIR spectra is not straightforward because there are many sources of peak shift and splitting (number of bridging oxygen), transversal/longitudinal vibrational modes, and size of the SiO_4 rings. A possible interpretation is that the δ ($\approx 1170\ cm^{-1}$) and γ ($\approx 1070\ cm^{-1}$) components are related to the Q^4 units (i.e., Si bonded to four bridging oxygen), including the effect of disorder-induced modes.[49] The lower energy vibrational features can be likely ascribed to Si—NBO bonds,[24,47,60] NBO being nonbridging oxygen. In particular, β ($\approx 970\ cm^{-1}$) can be attributed to Q^3 units whereas α ($\approx 920\ cm^{-1}$) might be related either to a band splitting due to transverse and longitudinal vibrational modes of the Q^3 band or to Q^2 units. We believe that the second interpretation is more convincing because the intensity of α decreases after FAIE, whereas β increases. Certainly, the structural reorganization of the glass is more relevant when ion exchange takes place on the tin side and this reflects the presence of electrochemical reactions causing variations in the oxidation state and coordination of Sn and Ag.

The structural/microstructural differences between FAIE on the tin and air side influence the optical properties of the exchanged glasses (Figure 7). The brownish coloration observed in the materials exchanged on the tin side is typically encountered when metallic nanocrystalline Ag (nc-Ag) forms within a glassy matrix,[61] although none of the spectra show sharp absorption features *in* the 410–450 nm range where the surface plasmon absorption of nc-Ag typically falls.[37,61–63] The absence of a clear plasmon peak is probably related to the broad distribution of the particle size.

The differences (tin vs air side) in the optical luminescence observed under UV radiation after ion exchange are also strictly related to the chemical environment of Ag, whose ions organize in luminescent pairs and small clusters.[17] Noteworthy, when glasses exchanged on air and tin side are compared, their luminescence appears difference also shedding the UV light from the "back" (i.e., from the nonexchanged face); this difference is very clear for silver penetration up to $\approx 10\ \mu m$ (2 min, 5 mA cm^{-2}). This points out that tin diffusion inside the glass modifies the environment of silver at least up to 10 μm beneath the surface. On the other hand, the luminescence becomes rather similar on both air and tin side when irradiated from the nonexchanged surface after 5 min under 5 mA cm^{-2} ($>20\ \mu m$ penetration), thus revealing that Sn only marginally changes the environment of silver ions at that depth.

Field-assisted Ag → Na ion exchange leads to an improved resistance to flaws formation, whereas no substantial changes are observed in terms of hardness and elastic modulus. Therefore, the reduced crack formation probability cannot be ascribed to modification of the elastic properties or hardness but could be attributed to the development of compressive residual stresses beneath the glass surface whose penetration increases with the treating time, or partially to an increase plasticity of the glass structure. However, the measured crack formation probabilities are substantially larger than those reported by Hassani[64] on the same glass after conventional K → Na ion exchange. In fact, the ionic volume difference between K$^+$ and Na$^+$ is much larger than that between Ag$^+$ and Na$^+$,[65] thus leading to lower surface compression in the case of Ag → Na

exchange. For instance, Shaisha and Cooper[66] measured the residual stress in soda–lime glass after field-assisted ion exchange using different diffusing ions. They found residual stresses <200 MPa after Ag → Na exchange, whereas more than 700 MPa were detected in the glasses exchanged with K. We can also observe that the differences between the samples treated on air and tin side are not statistically significant. The result appears consistent with the fact that 1) only a limited portion of the exchanged silver ions is reduced even on the tin side surface (<20% assuming a concentration for Sn^{4+} = 1 at%) and 2) such reduction is concentrated in the very thin layer beneath the surface where Tin is expected to diffuse.[40] For this reason, the differences in hardness and elastic modulus between the two sides are quite limited.

4. Conclusions

Solid-state field-assisted ion exchange allows fast diffusion of silver into SLS glass. The diffusion process is driven by the electric field and not by the concentration gradient as testified by non-Fickian diffusion profiles. We observe penetrations of $\approx 0.8\ \mu m\ min^{-1}\ (mA\ cm^{-2})^{-1}$ both on the air and tin side. The ion-exchanged region is characterized by superior resistance to crack formation, whereas surface hardness and elastic modulus remain practically unchanged. Conversely, the structural/microstructural features differ when ion exchange takes place on the air or tin side. In particular, a relevant amount of metallic silver nanocrystals forms on the tin side ($\approx 6\ nm$ on the surface without any postannealing treatment) and a deep structural rearrangement is observed. Moreover, results from Raman profiling show how this treatment influences the silver clustering process with particular regard to the size distribution of the Ag nanoparticles within the glass layers. While the impact on the mechanical properties of Ag nanoparticles formation is modest, the optical properties are strongly affected.

5. Experimental Section

Commercially available SLS float glass was used in this work. Its nominal composition is (wt%): 71.4 SiO_2; 1.0 Al_2O_3; 13.9 Na_2O; 0.3 K_2O; 4.1 MgO; 9.1 CaO; 0.2 others. The glass transition temperature was previously evaluated by dilatometry,[67] resulting in 611 °C. Tin and air sides were identified by observing the typical "milky" fluorescence of tin under UVC light irradiation.

The sheet (4 mm thick) was cut to obtain $\approx 20 \times 20\ mm^2$ square samples which were carefully cleaned using acetone (Sigma–Aldrich) in an ultrasonic bath for 5 min. Then, a square $\approx 10 \times 10\ mm^2$ was painted in the center of each specimen using silver paste (Toyobo DW-250 H-5). Some samples were painted on the tin side, others on the air side. A thin Cu wire was connected to the silver paint and the specimens were heat-treated at 400 °C for 15 min to consolidate and dry the paste (Nabertherm muffle furnace).

Field-assisted ion exchange process has already been described in detail elsewhere.[68] The samples were introduced in a stainless steel vessel (the nonpainted side of the samples facing the vessel) which was heated from the bottom by a hot plate. Additional heating was provided by a heating gun blowing hot air on the upper part of the specimens. A K-thermocouple in contact with the samples was used to check their temperature which was kept at 380 ± 10 °C. The stainless steel vessel was connected to the negative terminal of a DC power source

(Glassman 5 kV–120 mA) whereas the copper wire contacting the silver paste was connected to the positive one. The electric parameters during the process were checked using a digital multimeter Keithley 2100. The experiments were carried out in constant-current mode applying 5 mA cm^{-2} for different times (0.5–5 min). Additional experiments with larger current densities (10 and 20 mA mm^{-2}) were carried out only on the tin side for comparison.

The silver concentration profiles were evaluated by energy-dispersive X-ray spectroscopy (EDXS) line scans on fresh fracture surfaces using SEM Jeol JSM5500 equipped with EDS2000, IXRF System. The penetration depth was assumed as the distance from the surface where the Ag concentration was 5% of the surface one. Before EDXS, the samples were coated with a thin Pt–Pd film.

XRD was carried out using an Italstructures IPD3000 diffractometer, equipped with a Cu anode operating at 40 kV and 30 mA.

Raman microspectroscopy measurements were carried out in back-scattering geometry using a triple-axis monochromator (Horiba Jobin-Yvon, model T-64 000) set in the double subtractive/single configuration. The scattered radiation was filtered by three holographic gratings (1800 lines mm^{-1}) and detected by a CCD detector (1024 × 256 pixels) cooled by liquid nitrogen. The exciting radiation was provided by a mixed Ar–Kr ion gas laser (Spectra Physics, model Satellite 2018 RM) set at 514.5 nm. The laser beam was focused onto a spot of about 1 μm by a long working distance (LWD) Olympus objective (magnification 80× and NA = 0.75) and the scattered light was collected in confocal mode with the same objective. In-depth profiling analysis was done by recording the low-wavenumber Raman scattering spectra along the Z axis of the sample holder stage, starting from the surface of the exchanged glass slide and moving inward by steps of about 1 μm. The power on the sample surface was fixed at about 3 mW. Measurements were done at room temperature from samples in the air. Micro-Raman spectra were recorded in crossed (HV) polarization in the Stokes side, within the wavenumber region between 5 and 665 cm^{-1}, with an average spectral resolution of about 0.6 cm^{-1} pixel^{-1}. In the aim to carry out an accurate analysis of the very low-wavenumber region, each spectrum was corrected by subtracting the rotational Raman spectrum of air, occurring in the region below 180 cm^{-1} and a proper baseline, extending over the full spectral range, to account for the luminescence background. To avoid any effect of eventual instrumental drifts, some sharp lines originating either from secondary emission of plasma or from a calibrated argon lamp were used as reference through all the measurements. The spectra were analyzed within the elastic continuum approximation,[57,69,70] assuming that the observed Raman intensity $I^{obs}(\omega)$ is connected to the continuum density of states (DOS) $g(\omega)$. In fact, according to the Shuker and Gammon's procedure,[71] we obtain the reduced intensity $I^{red}(\omega)$ for the Stokes side of the HV spectra as follows

$$I^{red}(\omega) = \frac{I^{obs}(\omega)}{\omega[n(\omega,T)+1]} = C(\omega)\frac{g(\omega)}{\omega^2} \qquad (6)$$

In other words, the correction of the experimental Stokes component $I^{obs}(\omega)$ for the Bose–Einstein thermal population factor $[n(\omega,T)+1]$ gives a Raman intensity proportional to the vibrational density of states (VDOS) $g(\omega)/\omega^2$ divided by ω^2 through the light-to-vibrations coupling function $C(\omega)$.

The electron microscopy analyses were performed on a JEOL 2100 FEG S/TEM microscope operating at 200 kV and equipped with a probe spherical aberration corrector. Before the observation, thin areas of the specimens under study were obtained by ultramicrotomy.

FTIR spectra were acquired in ATR mode using a SpectraTech Inspect IR Plus facility (Si crystal) equipped with MCT-A detector.

Pictures of the ion-exchanged samples were collected with a Canon EOS-750D digital camera under visible and UV light. The absorbance spectra were collected with a UV–vis–NIR spectrophotometer (Jasco V770) at 200 nm min^{-1} in the wavelength range 300–700 nm.

The crack formation probability after ion exchange was evaluated using a FUTURE-TECH FM-310 microhardness tester equipped with a Vickers diamond indenter. Indentations were produced at different loads (25–2000 g) with dwell time of 10 s. At least ten indentations were considered per each loading condition and the number of cracks at the indentation corners was counted 2 min later.

Nanoindentation measurements were performed on Anton Paar NHT2 Nanoindentation Tester with Berkovich diamond indenter using instrumented technique (according to ISO 14 577 standard). The area function was calibrated on fused silica using standard procedure. Maximum loads of 5 and 50 mN were chosen (in order to verify that the mechanical response did not vary with the penetration depth). Loading time was 30 s followed by 10 s hold at the maximum load and unloading time 30 s. Twenty-five indentations were performed for both maximum loads on each sample. The hardness and Young's modulus were evaluated through the Oliver–Pharr method,[72] assuming Poisson's ratio equal to 0.2.

Supporting Information

Supporting Information is available from the Wiley Online Library or from the author.

Conflict of Interest

The authors declare no conflict of interest.

Data Availability Statement

The data that support the findings of this study are available from the corresponding author upon reasonable request.

[1] A. K. Varshneya, in *Fundamentals of Inorganic Glasses*, Academic Press, Inc., Cambridge, MA **1994**.

[2] P. Mazzoldi, S. Carturan, A. Quaranta, C. Sada, *Riv. Del Nuovo Cim.* **2013**, *36*, 397.

[3] C. Balagna, S. Perero, E. Percivalle, E. V. Nepita, M. Ferraris, *Open Ceram.* **2020**, *1*, 100006.

[4] J. S. Kim, E. Kuk, K. N. Yu, J.-H. Kim, S. J. Park, H. J. Lee, S. H. Kim, Y. K. Park, Y. H. Park, C.-Y. Hwang, Y.-K. Kim, Y.-S. Lee, D. H. Jeong, M.-H. Cho, *Nanomed. Nanotechnol. Biol. Med.* **2007**, *3*, 95.

[5] D. Guldiren, S. Aydın, *Mater. Sci. Eng. C* **2017**, *78*, 826.

[6] N. F. Borrelli, W. Senaratne, Y. Wei, O. Petzold, *ACS Appl. Mater. Interfaces* **2015**, *7*, 2195.

[7] D. Guldiren, S. Aydin, *Mater. Sci. Eng. C* **2016**, *67*, 144.

[8] D. Guldiren, İ. Erdem, S. Aydin, *J. Non. Cryst. Solids* **2016**, *441*, 1.

[9] T. Findakly, *Opt. Eng.* **1985**, *24*, 242244.

[10] B. Pantchev, Z. Nikolov, *IEEE J. Quantum Electron.* **1993**, *29*, 2459.

[11] G. Stewart, C. Millar, P. Laybourn, C. Wilkinson, R. DelaRue, *IEEE J. Quantum Electron.* **1977**, *13*, 192.

[12] A. K. Varshneya, *Int. J. Appl. Glas. Sci.* **2010**, *1*, 131.

[13] E. Cattaruzza, V. M. Caselli, M. Mardegan, F. Gonella, G. Bottaro, A. Quaranta, G. Valotto, F. Enrichi, *Ceram. Int.* **2015**, *41*, 7221.

[14] J. Zhao, J. Zhu, Z. Yang, Q. Jiao, C. Yu, J. Qiu, Z. Song, *J. Am. Ceram. Soc.* **2020**, *103*, 955.

[15] F. Gonella, *Ceram. Int.* **2015**, *41*, 6693.

[16] A. Simo, J. Polte, N. Pfänder, U. Vainio, F. Emmerling, K. Rademann, *J. Am. Chem. Soc.* **2012**, *134*, 18824.

[17] A. Quaranta, A. Rahman, G. Mariotto, C. Maurizio, E. Trave, F. Gonella, E. Cattaruzza, E. Gibaudo, J. E. Broquin, *J. Phys. Chem. C* **2012**, *116*, 3757.

[18] E. Borsella, G. Battaglin, M. A. Garcìa, F. Gonella, P. Mazzoldi, R. Polloni, A. Quaranta, *Appl. Phys. A* **2000**, *71*, 125.

[19] A. Talimian, G. Mariotto, V. M. Sglavo, *Int. J. Appl. Glas. Sci.* **2017**, *8*, 291.

[20] H. Kawamura, R. Suzuki, S. Matsusaka, H. Hidai, A. Chiba, N. Morita, *Precis. Eng.* **2019**, *55*, 240.

[21] R. Oven, M. Yin, P. A. Davies, *J. Phys. D: Appl. Phys.* **2004**, *37*, 2207.

[22] Y. Ma, J. Lin, S. Qin, N. Zhou, Q. Bian, H. Wei, Z. Feng, *Solid State Sci.* **2010**, *12*, 1413.

[23] B. Okorn, I. Fabijanić, J. Sancho-Parramon, F. Zupanič, T. Bončina, V. Janicki, *Thin Solid Films* **2019**, *685*, 402.

[24] N. Takamure, A. Kondyurin, D. R. McKenzie, *J. Appl. Phys.* **2019**, *125*, 175104.

[25] E. Borsella, E. Cattaruzza, G. De Marchi, F. Gonella, G. Mattei, P. Mazzoldi, A. Quaranta, G. Battaglin, R. Polloni, *J. Non. Cryst. Solids* **1999**, *245*, 122.

[26] X. Yang, Z. Li, W. Li, J. Xu, Z. Dong, S. Qian, *Chinese Sci. Bull.* **2008**, *53*, 695.

[27] J. P. Blondeau, F. Catan, C. Andreazza-Vignolle, N. Sbai, *Plasmonics* **2008**, *3*, 65.

[28] E. Borsella, G. De Marchi, F. Caccavale, F. Gonella, G. Mattei, P. Mazzoldi, G. Battaglin, A. Quaranta, A. Miotello, *J. Non. Cryst. Solids* **1999**, *253*, 261.

[29] J. Sancho-Parramon, V. Janicki, P. Dubček, M. Karlušić, D. Gracin, M. Jakšić, S. Bernstorff, D. Meljanac, K. Juraić, *Opt. Mater.* **2010**, *32*, 510.

[30] A. A. Menazea, A. M. Abdelghany, *Radiat. Phys. Chem.* **2020**, *174*, 108958.

[31] G. Medhi, P. Nandi, S. Mohan, G. Jose, *Mater. Lett.* **2007**, *61*, 2259.

[32] M. Dubiel, R. Schneider, H. Hofmeister, K.-D. Schicke, J. C. Pivin, *Eur. Phys. J. D* **2007**, *43*, 291.

[33] K. Tanabe, *Mater. Lett.* **2007**, *61*, 4573.

[34] A. Ciesielski, K. M. Czajkowski, D. Switlik, *Sol. Energy* **2019**, *184*, 477.

[35] P. K. Jain, X. Huang, I. H. El-Sayed, M. A. El-Sayed, *Acc. Chem. Res.* **2008**, *41*, 1578.

[36] E. Cattaruzza, M. Mardegan, T. Pregnolato, G. Ungaretti, G. Aquilanti, A. Quaranta, G. Battaglin, E. Trave, *Sol. Energy Mater. Sol. Cells* **2014**, *130*, 272.

[37] M. V. Shestakov, M. Meledina, S. Turner, V. K. Tikhomirov, N. Verellen, V. D. Rodríguez, J. J. Velázquez, G. Van Tendeloo, V. V. Moshchalkov, *J. Appl. Phys.* **2013**, *114*, 073102.

[38] M. Ferrari, F. Gonella, M. Montagna, C. Tosello, *J. Appl. Phys.* **1996**, *79*, 2055.

[39] B. Yang, P. D. Townsend, S. A. Holgate, *J. Phys. D: Appl. Phys.* **1994**, *27*, 1757.

[40] G. H. Frischat, *Comptes Rendus Chim.* **2002**, *5*, 759.

[41] P. D. Townsend, N. Can, P. J. Chandler, B. W. Farmery, R. Lopez-Heredero, A. Peto, L. Salvin, D. Underdown, B. Yang, *J. Non. Cryst. Solids* **1998**, *223*, 73.

[42] X. Li, L. Jiang, Y. Wang, I. Mohagheghian, J. P. Dear, L. Li, Y. Yan, *J. Non. Cryst. Solids* **2017**, *471*, 72.

[43] L. Jiang, X. Guo, X. Li, L. Li, G. Zhang, Y. Yan, *Appl. Surf. Sci.* **2013**, *265*, 889.

[44] H. Hassani, V. M. Sglavo, *J. Non. Cryst. Solids* **2019**, *515*, 143.

[45] Pilkington, NSG Glanova, https://www.pilkington.com/en/global/digital-signage/products/applications/uncoated-ultrathin-cover-glass-for-touch-screens-and-displays/nsg-glanova (accessed: February, 2021).

[46] Glass on Web, Pilkington North America Exhibiting at the SID Display Week **2019**, https://www.glassonweb.com/news/pilkington-north-america-exhibiting-sid-display-week-2019 (accessed: February, 2021).

[47] J. Lao, X. Dieudonné, M. Benbakkar, É. Jallot, *J. Mater. Sci.* **2017**, *52*, 9129.

[48] A.-M. Putz, M. Putz, *Int. J. Mol. Sci.* **2012**, *13*, 15925.

[49] P. Innocenzi, *J. Non. Cryst. Solids* **2003**, *316*, 309.

[50] C. T. Mclaren, C. Kopatz, N. J. Smith, H. Jain, *Sci. Rep.* **2019**, *9*, 2805.

[51] L. Pinter, M. Biesuz, V. M. Sglavo, T. Saunders, J. Binner, M. Reece, S. Grasso, *Scr. Mater.* **2018**, *151*, 14.

[52] M. Biesuz, M. Cipriani, V. M. Sglavo, G. D. Sorarù, *Scr. Mater.* **2020**, *182*, 94.

[53] G. Pintori, V. M. Sglavo, *J. Non. Cryst. Solids* **2022**, *600*, 121994.

[54] A. Tamura, K. Higeta, T. Ichinokawa, *J. Phys. C* **1982**, *15*, 4975.

[55] E. Duval, A. Boukenter, B. Champagnon, *Phys. Rev. Lett.* **1986**, *56*, 2052.

[56] H. Lamb, *Proc. London Math. Soc.* **1882**, *13*, 51.

[57] M. Ferrari, L. M. Gratton, A. Maddalena, M. Montagna, C. Tosello, *J. Non. Cryst. Solids* **1995**, *191*, 101.

[58] I. Barin, in *Thermochemical Data of Pure Substances*, VCH Verlagsgesellschaft MbH and VCH Publishers, Inc., Weinheim, Germany **1995**.

[59] J. Assal, B. Hallstedt, L. J. Gauckler, *J. Am. Ceram. Soc.* **2005**, *80*, 3054.

[60] N. Sheth, J. Luo, J. Banerjee, C. G. Pantano, S. H. Kim, *J. Non. Cryst. Solids* **2017**, *474*, 24.

[61] P. Kumar, M. C. Mathpal, A. K. Tripathi, J. Prakash, A. Agarwal, M. M. Ahmad, H. C. Swart, *Phys. Chem. Chem. Phys.* **2015**, *17*, 8596.

[62] A. Campos, N. Troc, E. Cottancin, M. Pellarin, H.-C. Weissker, J. Lermé, M. Kociak, M. Hillenkamp, *Nat. Phys.* **2019**, *15*, 275.

[63] Y. M. Sgibnev, N. V. Nikonorov, A. I. Ignatiev, *J. Lumin.* **2017**, *188*, 172.

[64] H. Hassani, in *Structure Evolution and Mechanical Properties of Ion-Exchanged Silicate Glass*, University of Trento, Trento **2019**.

[65] Y.-M. Chiang, D. Birnie, P. W. D. Kingery, in *Physical Ceramics: Principles for Ceramic Science and Engineering*, Wiley, Hoboken, NJ **1997**.

[66] E.E. Shaisha, A.R. Cooper, *J. Am. Ceram. Soc.* **1981**, *64*, 278.

[67] M. Biesuz, M. Cipriani, V. M. Sglavo, G. D. Sorarù, *Scr. Mater.* **2020**, *182*, 94.

[68] M. Biesuz, P. Giopato, F. Tessarolo, G. Nollo, M. Bortolotti, V. M. Sglavo, G. D. Sorarù, *J. Eur. Ceram. Soc.* **2021**, *41*, 3755.

[69] M. Montagna, R. Dusi, *Phys. Rev. B* **1995**, *52*, 10080.

[70] M. Ivanda, A. M. Tonejc, I. Djerdj, M. Gotić, S. Musić, G. Mariotto, M. Montagna, in *Res.*, Springer Berlin Heidelberg, Berlin **2008**, p. 24.

[71] R. Shuker, R. W. Gammon, *Phys. Rev. Lett.* **1970**, *25*, 222.

[72] W. C. Oliver, G. M. Pharr, *J. Mater. Res.* **1992**, *7*, 1564.